

Electrochemical generation of liquid and solid sulfur on two-dimensional layered materials with distinct areal capacities

Ankun Yang^{1,10}, Guangmin Zhou^{1,10}, Xian Kong², Rafael A. Vilá¹, Allen Pei¹, Yecun Wu³, Xiaoyun Yu¹, Xueli Zheng¹, Chun-Lan Wu¹, Bofei Liu¹, Hao Chen¹, Yan Xu¹, Di Chen^{1,9}, Yanxi Li¹, Sirine Fakra⁴, Harold Y. Hwang^{5,6}, Jian Qin², Steven Chu^{7,8} and Yi Cui^{1,6*}

It has recently been shown that sulfur, a solid material in its elementary form S_8 , can stay in a supercooled state as liquid sulfur in an electrochemical cell. We establish that this newly discovered state could have implications for lithium–sulfur batteries. Here, through in situ studies of electrochemical sulfur generation, we show that liquid (supercooled) and solid elementary sulfur possess very different areal capacities over the same charging period. To control the physical state of sulfur, we studied its growth on two-dimensional layered materials. We found that on the basal plane, only liquid sulfur accumulates; by contrast, at the edge sites, liquid sulfur accumulates if the thickness of the two-dimensional material is small, whereas solid sulfur nucleates if the thickness is large (tens of nanometres). Correlating the sulfur states with their respective areal capacities, as well as controlling the growth of sulfur on two-dimensional materials, could provide insights for the design of future lithium–sulfur batteries.

Sulfur is an attractive cathode material due to its high specific capacity ($1,675 \text{ mA h g}^{-1}$) and low cost. Therefore, lithium–sulfur (Li–S) batteries have high energy density and show promise for use in electric vehicles and grid-scale energy storage¹. However, challenges, including short cycle life and poor Coulombic efficiency, still exist in Li–S batteries despite extensive studies in recent years². The primary underlying reasons for this include the following²: (1) the solubility of the lithium polysulfide intermediates (Li_2S_n , $3 \leq n \leq 8$) leads to a ‘shuttle effect’ and causes rapid capacity fading, and (2) the charge and discharge products, sulfur (S_8) and lithium sulfide (Li_2S), respectively, are electrically insulating, resulting in the inefficient utilization of the active materials. To understand the reaction processes and achieve better designs of Li–S batteries, ex situ studies, including scanning electron microscopy (SEM), transmission electron microscopy (TEM) and X-ray diffraction (XRD), are commonly used to examine the structural and morphological changes of the sulfur species and/or identify their binding strengths with different cathode materials^{3–5}. At the same time, new approaches and tools, especially in situ or operando microscopy and spectroscopy methods, including optical microscopy⁶, transmission X-ray microscopy⁷ and X-ray absorption spectroscopy (XAS)^{8,9}, are gaining increasing attention for monitoring and uncovering the reactions and processes of batteries as they provide more reliable information in real time¹⁰. However, most of the research has been focused on the intermediate polysulfides and the discharge product lithium sulfide (Li_2S), with much less research on the charge product sulfur (S_8).

We recently discovered a surprising and important phenomenon in our in situ studies: the charge product sulfur, commonly

believed to be solid^{4,8}, can stay in a supercooled liquid state on metallic substrates at room temperature, which is well below the melting temperature of sulfur (115°C)⁶. We found that these metastable supercooled liquid sulfur droplets quickly solidify upon contact with crystalline sulfur. It is well known that liquids, in contrast to solids, have flowability and adaptive capabilities due to weaker interatomic interactions. Thus, in the context of Li–S electrochemistry, how the state (liquid or solid) of sulfur affects the cathodic behaviour and the energy storage performance become important questions. On the other hand, two-dimensional (2D) layered materials, including metal sulfides (MoS_2 (refs. ^{5,11,12}), WS_2 (ref. ¹³), TiS_2 (ref. ¹⁴) and others^{15,16}), graphene and graphene oxides^{17–21}, and black phosphorus²², have received increasing interest for their use in Li–S batteries to enhance the conductivity of cathode materials and/or trap polysulfides. However, how sulfur interacts with these 2D layered materials has not been widely studied.

Here we present the first in situ study of the electrochemical generation of sulfur on 2D layered materials and correlate the sulfur state (liquid or solid) with the electrochemical performance. First, we set up an optical cell that allows real-time electrochemical control and in situ optical imaging of sulfur generation. We show that sulfur prefers to grow as liquid droplets on the basal plane (flat top surface) of 2D layered materials and crystallize from the edges. We explain the distinct growth behaviours through a combination of factors, including binding energy, wetting, electric field distribution and critical nucleus size. Second, by understanding edge-induced crystallization, we can control the sulfur state (liquid or solid) on 2D materials and demonstrate that liquid sulfur provides a much

¹Department of Materials Science and Engineering, Stanford University, Stanford, CA, USA. ²Department of Chemical Engineering, Stanford University, Stanford, CA, USA. ³Department of Electrical Engineering, Stanford University, Stanford, CA, USA. ⁴Advanced Light Source, Lawrence Berkeley National Laboratory, Berkeley, CA, USA. ⁵Department of Applied Physics, Stanford University, Stanford, CA, USA. ⁶Stanford Institute for Materials and Energy Sciences, SLAC National Accelerator Laboratory, Menlo Park, CA, USA. ⁷Department of Physics, Stanford University, Stanford, CA, USA. ⁸Department of Molecular and Cellular Physiology, Stanford University, Stanford, CA, USA. ⁹Present address: The Future Laboratory, Tsinghua University, Beijing, China. ¹⁰These authors contributed equally: Ankun Yang, Guangmin Zhou. *e-mail: yicui@stanford.edu

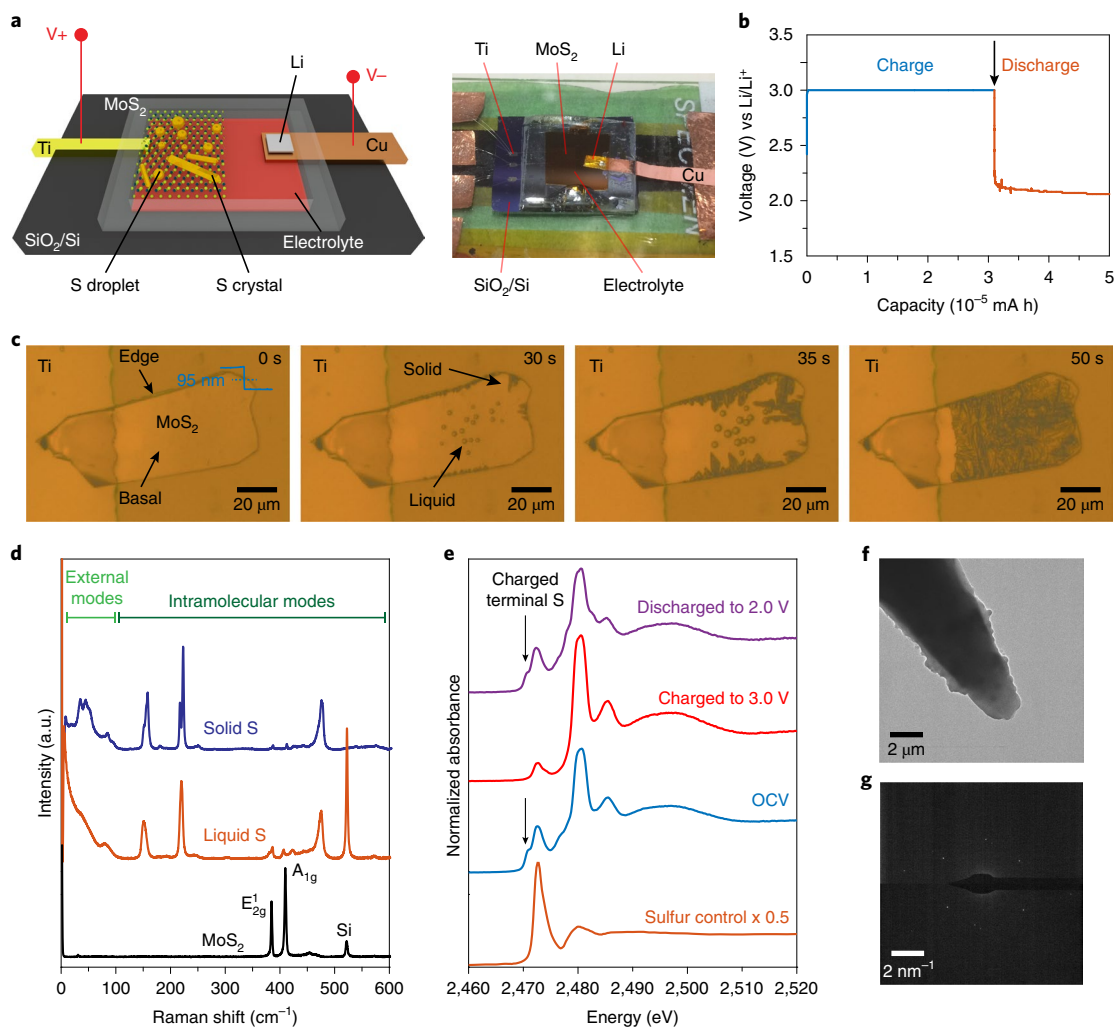


Fig. 1 | Electrochemical generation of liquid and solid sulfur on MoS₂. **a**, The in situ optical cell used to perform the electrochemical generation of sulfur that enables simultaneous optical detection and electrochemical measurement. Left: schematic; right: a photo of the device. V+ and V– indicate that a positive voltage is applied on MoS₂ versus Li. **b**, The electrochemical cell was first charged at a constant voltage of 3.0 V (overpotential $\eta = 0.6$ V) and then galvanostatically discharged at a current of 0.001 mA. **c**, In situ bright-field optical microscopy images show the evolution of sulfur generation on the MoS₂ flake. **d**, The in situ Raman spectra of liquid and solid sulfur on MoS₂ both show intramolecular Raman modes of S₈ as well as signatures of MoS₂. In the low-frequency range, liquid sulfur exhibits a wing feature whereas solid sulfur shows distinct external modes. **e**, In situ S K-edge XANES spectra confirming the composition of liquid sulfur. At open-circuit voltage (OCV), the two absorption peaks at 2,471 eV and 2,473 eV originate from polysulfides and correspond to negatively charged terminal sulfur atoms and neutral internal sulfur atoms, respectively. When charged to 3.0 V, the absorption peak at 2,471 eV disappears, indicating the conversion of S₂²⁻ into elemental sulfur. The remaining absorption feature at 2,473 eV matches that of the sulfur control. The absorption features at 2,481 and 2,486 eV are from lithium bis(trifluoromethanesulfonyl)imide in the electrolyte⁹. **f, g**, cryo-EM image (**f**) and SAED pattern (**g**) confirming the crystallinity of solid sulfur.

higher capacity than solid sulfur in the same charge period. Unlike solid sulfur crystal, liquid sulfur droplets have high mobility and reshaping capability, do not block the electrolyte from accessing the electrode surface and thus achieve good kinetics during battery operation. Finally, we demonstrate that these sulfur growth behaviours are also observed on other 2D layered materials. With the universality of the phenomenon, the results shown here provide insights for the design of advanced electrodes as well as the utilization of 2D layered materials for high-performance Li–S batteries.

Electrochemical generation of liquid and solid sulfur

We designed an optical cell (Fig. 1a) to perform the electrochemical generation of sulfur on 2D materials. We chose micrometre-scale 2D flakes (usually 1–100 μm in lateral size and 1–100 nm in thickness) as the sulfur growth substrates because they are flat crystalline,

amenable to microfabrication techniques and can be easily integrated into devices and investigated by non-invasive optical microscopy. The optical cell consisted of MoS₂ (or other 2D flakes) as the working electrode, lithium scratched onto a copper foil as the counter electrode and polysulfides in 1,3-dioxolane/1,2-dimethoxyethane as the electrolyte. All the components were placed between a SiO₂/Si substrate and a transparent cover glass slide and sealed with a thermoplastic film to enable in situ optical observation (see Methods). We screened the common metals and selected titanium to build the electrode on MoS₂ because sulfur does not grow on titanium, and will be generated only on MoS₂. A typical MoS₂ flake prepared by mechanical exfoliation was used here as an example, with a thickness of 95 nm measured by atomic force microscopy (AFM). The open-circuit voltage of the device was around 2.4 V and a constant voltage of 3.0 V was applied to electrochemically generate

sulfur (Fig. 1b). The polysulfide (Li_2S_n , $3 \leq n \leq 8$) was oxidized to produce elemental sulfur: $\text{S}_x^{2-} - 2e^- \rightarrow x/8\text{S}_8$, $x = 3-8$.

Figure 1c shows snapshots of the sulfur generation on MoS_2 at 3.0 V as a function of charge time (Supplementary Movie 1). These bright-field optical images show distinct sulfur growth behaviours on the basal plane and edges of MoS_2 . Specifically, liquid sulfur droplets grew on the basal plane whereas solid sulfur formed at the edges. The solid sulfur quickly expanded across the basal plane of MoS_2 to cover the whole MoS_2 flake completely. The solid sulfur grew towards the centre of the MoS_2 flake where sulfur was produced by the oxidation of polysulfides. When MoS_2 lies on a conducting substrate or there are nearby flakes, solid sulfur can also grow outwards (Supplementary Fig. 1). The solid sulfur underwent only a slight morphology change over time and dissolved upon release of the voltage (Supplementary Fig. 2). In situ Raman spectroscopy confirmed the formation of sulfur on MoS_2 (Fig. 1d). Both the liquid and solid sulfur on MoS_2 show intramolecular Raman features at 150, 220 and 473 cm^{-1} , corresponding to the asymmetric S–S bending mode, the symmetric S–S bending mode and the S–S stretching mode, respectively. Raman signatures from MoS_2 were also observed. The low-frequency Raman spectra between 10 and 100 cm^{-1} exhibit several modes for solid sulfur, but only a Rayleigh wing feature for liquid sulfur. These distinct Raman features match those of commercial crystalline sulfur and molten sulfur (Supplementary Fig. 3), indicating that the generated solid sulfur is crystalline and the liquid sulfur is amorphous²³. Due to the difference in crystallinity, liquid sulfur exhibits a polarization-dependent optical response whereas liquid sulfur does not (Supplementary Figs. 4 and 5). Although we cannot exclude the possibility of Raman-inactive impurities, we believe their concentration should be low based on our previous results⁶.

To further confirm the composition of the liquid droplets, we performed in situ sulfur K-edge X-ray absorption near-edge structure (XANES) measurements (Fig. 1e and Supplementary Fig. 6a). At the open-circuit voltage of around 2.4 V, the XANES spectrum of the lithium polysulfides (Li_2S_x) exhibits two main absorption features, at 2,471 eV, due to the negatively charged terminal sulfur atoms, and 2,473 eV, due to the $x-2$ internal atoms in the polysulfide chain²⁴. When charged to 3.0 V, the absorption feature at 2,471 eV disappears whereas the feature at 2,473 eV remains, matching that of the sulfur control, indicating the complete conversion of S_x^{2-} into elemental sulfur. When discharged to about 2.0 V, the absorption feature at 2,471 eV reappears, implying the conversion of sulfur into S_x^{2-} . Combining in situ optical microscopy, which unambiguously shows liquid droplet generation (Supplementary Fig. 6b), and in situ XANES measurement, we conclude that the generated liquid droplets are composed of sulfur. On the other hand, solid sulfur is sensitive to electron beam irradiation and can easily sublime in high vacuum²⁵, therefore in most previous studies sulfur was encapsulated in carbon materials for TEM characterization^{3,26}. Here, for the first time, we employed cryogenic electron microscopy (cryo-EM) to probe the crystallinity of the solid sulfur. We successfully obtained the selected area electron diffraction (SAED) patterns, which demonstrated a high degree of crystallinity (Fig. 1fg and Supplementary Figs. 7 and 8), confirming that the S_8 molecules in solid sulfur have long-range order (Supplementary Movie 2), consistent with the in situ Raman spectroscopy measurements.

Mechanistic study of sulfur generation on 2D materials

To understand the different growth behaviours of sulfur on the basal plane and at the edges of MoS_2 , we first performed density functional theory (DFT) calculations to study the binding energy between S_8 and MoS_2 at the basal plane and the edges (Fig. 2a). We found that the binding energy between S_8 and the basal plane is very small (0.64 eV), and the weak binding likely leads to the formation of liquid sulfur droplets (Supplementary Fig. 9a). The formation of a

contact angle of $\sim 180^\circ$ suggests frustrated heterogeneous nucleation on the basal plane^{6,27}. At the edges, surprisingly, the binding energy is only slightly higher than that at the basal plane (0.66 eV). Sulfur binds to the molybdenum edge very intensely so that S_8 breaks into small sulfur molecules S_x ($x < 8$; Fig. 2a, inset). Afterwards, the binding between S_8 and the molybdenum edge is similar to that between S_8 and the sulfur edge. The small difference between the binding energies at the basal plane and the edges indicates that sulfur may appear as liquid droplets on both the basal plane and the edges in the initial stages. Indeed, we observed liquid sulfur droplets at the edges experimentally (Fig. 2e and Supplementary Movie 3). We note that at the edges of the MoS_2 flakes, the liquid droplets could be too small to be visualized by the diffraction-limited optical microscope until they turn into solid crystal. Therefore, we performed the same sulfur generation experiment on a vertical MoS_2 film that has molecular layers vertically aligned and exposes a large area of edges (Supplementary Fig. 10a). Interestingly, only liquid sulfur droplets were observed, indicating that the MoS_2 edges themselves do not necessarily cause the crystallization of sulfur. Similarly to the binding energy calculations, molecular dynamics (MD) simulations explicitly considering all components, including sulfur molecules, electrolyte and the MoS_2 substrate, showed that the sulfur molecules on the edges of a MoS_2 flake have slight tendency to wet the surface, without applying a potential (Fig. 2b).

When a constant potential (for example, 3.0 V) was applied, another important factor comes into play: the non-uniform distribution of the electric field on the 2D flake. The MoS_2 flakes exhibit strongly localized partial charges and an enhanced electric field at the edges upon applying a voltage (Fig. 2c,d and Supplementary Fig. 11), which will not only facilitate sulfur generation and local sulfur supersaturation, but also drive the wetting of the liquid sulfur droplets (Supplementary Figs. 12 and 13), similarly to the electrowetting phenomenon (Supplementary Fig. 9b)^{28,29}. Wetting can lower the nucleation barrier from liquid to solid, thus facilitating heterogeneous nucleation and crystallization of sulfur at the edges. Meanwhile, the van der Waals gaps and the edge sites of the 2D flakes may enable anchoring of S_8 molecules, which can act as seeds to facilitate the ordering of S_8 molecules into a solid crystal (Supplementary Fig. 14).

We observed a clear MoS_2 thickness dependence of sulfur crystallization at the MoS_2 edges. With decreasing flake thickness, it is more unlikely that sulfur will crystallize from the edges. We believe that sulfur cannot reach the critical nucleus size at the edge of thin 2D flakes. This hypothesis is proved on monolayer MoS_2 prepared by chemical vapour deposition (CVD; Fig. 2f). In contrast to MoS_2 with large thickness, only liquid sulfur droplets were observed on the basal plane of monolayer MoS_2 without crystallizing over a long time ($>1 \text{ h}$; Fig. 2f, Supplementary Fig. 10b,c and Supplementary Movie 4). These liquid droplets were initially small and coalesced into larger droplets. Although they are rooted to the flakes connected to titanium electrodes, the droplets may be larger than the flakes from a top-down view (Supplementary Fig. 10b). The size and areal number density of the sulfur droplets changed continuously but remained in the liquid phase during the observation time window (30–60 min). However, the liquid sulfur droplets are metastable and can transform into solid crystal in the presence of other growing sulfur crystal (Supplementary Fig. 15), similarly to the droplets on the basal plane of the thick MoS_2 flake (Fig. 1c). During discharging, the dissolution of liquid sulfur into polysulfides is generally fast, as a liquid/liquid transition (Supplementary Fig. 16). Surprisingly, liquid and solid sulfur can co-exist on MoS_2 flakes with different thicknesses connected to the same titanium electrode (Supplementary Fig. 17). This further confirms that the thickness of 2D materials, in addition to the edge effect, also plays a critical role in sulfur crystallization dictated by the critical nucleus size.

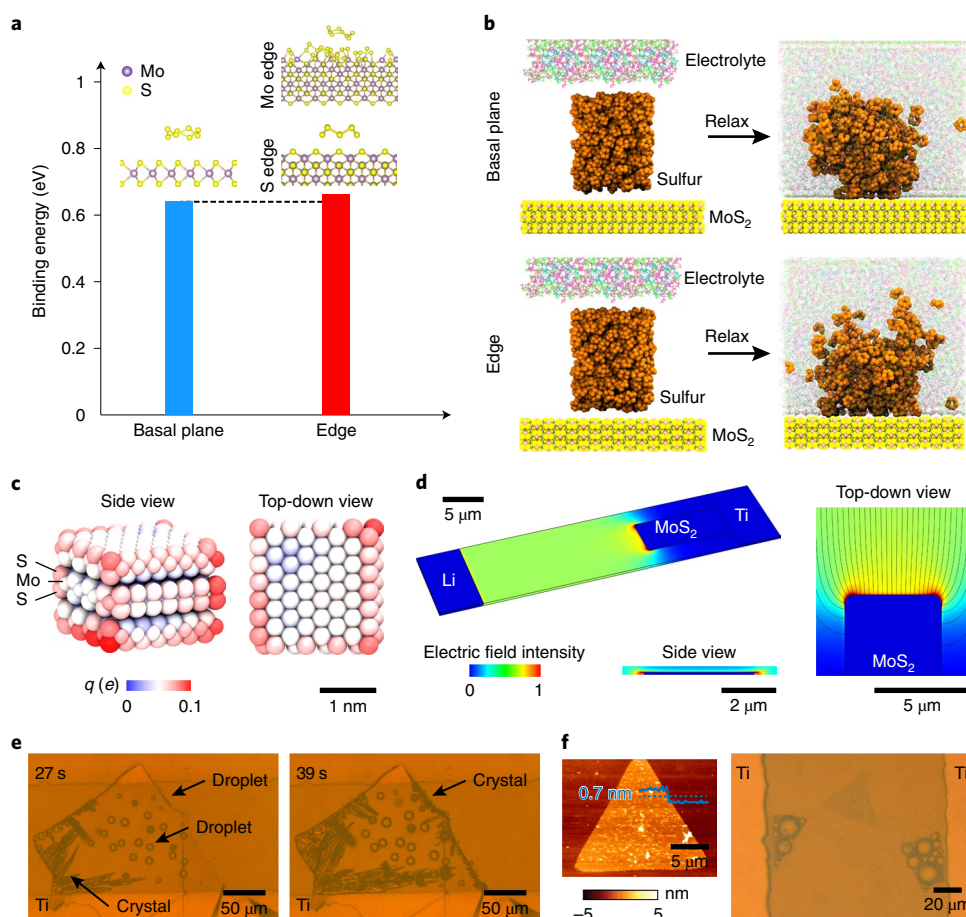


Fig. 2 | Mechanism of sulfur generation on MoS₂. **a**, The binding energy between S₈ and the edge of MoS₂ is slightly larger than the binding energy between S₈ and the basal plane of MoS₂. The images above the bar chart illustrate the corresponding interaction configurations. **b**, MD simulations show sulfur has a greater preference for wetting (occupying a larger surface) after relaxing on the edges of a MoS₂ flake (bottom panel) in comparison with on the basal plane (top panel). **c**, Atomic partial charges on a MoS₂ flake at a constant potential of 3.0 V show that the atoms located at the edges and corners carry more charge (scale bar is in units of elementary charge, e). **d**, The MoS₂ flake exhibits an enhanced electric field (normalized to the maximum value) at the edges. **e**, Observation of liquid sulfur droplets at the edges of MoS₂, indicated by the arrows, which quickly solidify. **f**, Left: a typical AFM image of a monolayer of MoS₂ showing a thickness of 0.7 nm. Right: optical image showing liquid sulfur droplets on the basal plane of a monolayer of MoS₂.

Correlating sulfur state with electrochemical performance

The distinct growth behaviour of sulfur, that is, into liquid droplets or solid crystal, provides an excellent opportunity to examine the correlation between sulfur state and electrochemical performance. We again took advantage of our planar battery design as it enables visualization of sulfur growth and electrochemical measurement simultaneously. One way to control the sulfur state is to suppress sulfur crystallization from the edges through titanium deposition. Specifically, the MoS₂ edges were covered with 80–100 nm titanium with only a part of the flake (15 μm × 15 μm) exposed by electron beam lithography or photolithography (Fig. 3a). Figure 3b shows two representative cells in which the edges of MoS₂ were either completely covered to suppress sulfur crystallization or left open to initiate sulfur crystallization. To exclude the capacity contribution from titanium electrodes due to adsorption of sulfur species and charge accumulation, we further deposited 120 nm SiO₂ to cover the titanium electrode. For cells with complete titanium coverage, liquid sulfur droplets were dynamically generated over time (Fig. 3c and Supplementary Movie 5). Some droplets increased in size at the expense of other droplets and new small droplets kept emerging. The sulfur droplets remained as liquid droplets and did not crystallize for at least 15 min. With the continuous electrochemical generation of sulfur droplets, the corresponding capac-

ity increased almost linearly over time to 8.0 mA h cm⁻² at 15 min (Fig. 3e). For cells with some edges exposed (with the same surface area of MoS₂), however, the liquid droplets on the MoS₂ surface quickly turned into solid crystal (at 25 s; Fig. 3d and Supplementary Movie 6). The crystal reconfigured to be flat on top of MoS₂ and then did not significantly change morphology over the course of the experiment (1–15 min). Compared with the liquid droplets, the solid crystal experienced a limited capacity increase, to only 1.9 mA h cm⁻² over 15 min, 76% less than the areal capacity of the liquid droplets. Comparison within exactly the same device (Supplementary Fig. 18) also clearly demonstrated that liquid and solid sulfur show distinct capacities. Notably, a change in the slope of the capacity/time curve of the solid sulfur crystal (Fig. 3e, indicated by an arrow in the enlarged view) is observed that matches the exact time when the state of sulfur changed from liquid to solid. This directly demonstrates a slow down of the kinetics. This phenomenon was observed consistently in different cells in which liquid sulfur turned into solid (Supplementary Fig. 19).

To further confirm the effect of sulfur state on the electrochemical performance, we designed devices that generate either liquid sulfur droplets or solid sulfur crystal at different applied voltages (3.0, 3.2 and 3.5 V). When liquid sulfur droplets grew on MoS₂ (Fig. 3f), the capacity increased almost linearly as a function

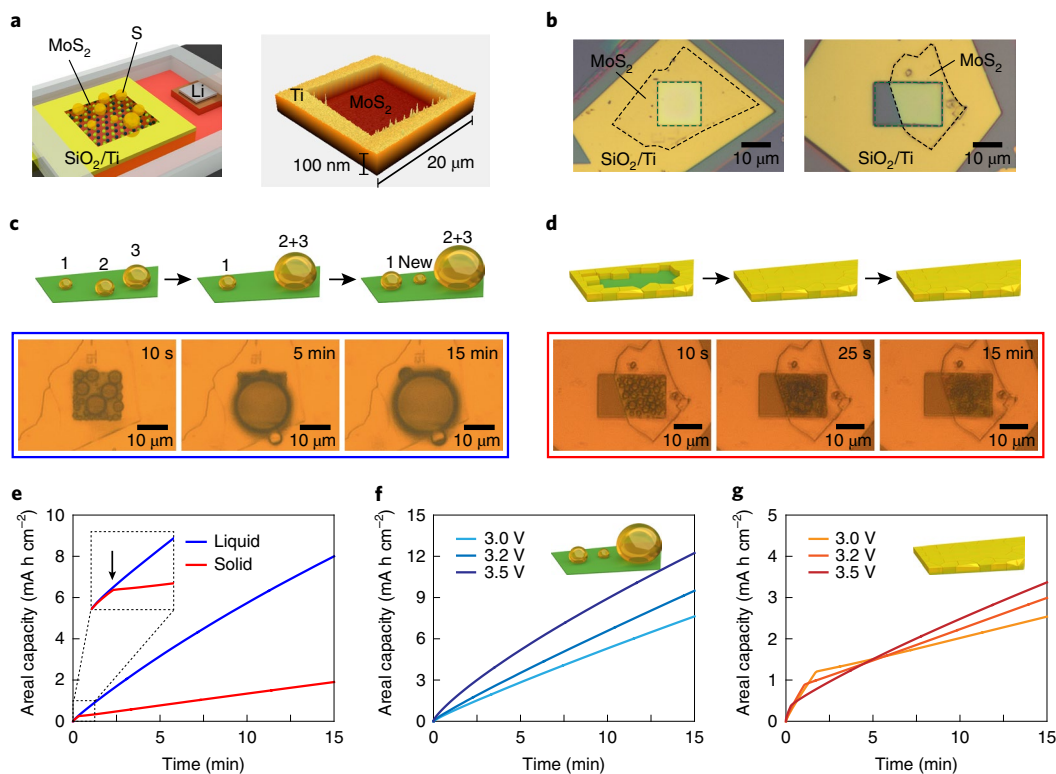


Fig. 3 | Correlating sulfur state with electrochemical performance. **a**, The experimental set-up shown as a schematic and an AFM image: a window ($15\ \mu\text{m} \times 15\ \mu\text{m}$) was designed on a MoS_2 flake to electrochemically generate sulfur. **b**, Two representative cells with the same exposed area of MoS_2 designed to generate liquid and solid sulfur, respectively. **c**, Cartoon and in situ optical microscopy images of a device showing the merging of the liquid droplets opens new active sites for emerging new droplets. **d**, Cartoon and in situ optical microscopy images of a device showing solid crystal occupying the surface of the MoS_2 flake, blocking further sulfur generation on the flake. **e**, The areal capacity of the devices shown in **c** and **d** as a function of time at 3.0 V. The inset shows the change in slope for the generation of solid sulfur, indicated by the arrow, in comparison with the generation of liquid sulfur. **f, g**, The areal capacity of devices generating either liquid (**f**) or solid (**g**) sulfur at different voltages as a function of time.

of time. Also, the capacities at 15 min were generally large, and increased from $7.6\ \text{mA h cm}^{-2}$ (3.0 V) to $9.5\ \text{mA h cm}^{-2}$ (3.2 V) and then to $12.2\ \text{mA h cm}^{-2}$ (3.5 V). A similar phenomenon was observed with the vertical MoS_2 devices, in which only liquid droplets were generated (Supplementary Fig. 20). In contrast, when the solid sulfur crystal grew on MoS_2 (Fig. 3g), the areal capacities at 15 min (2.5, 3.0 and $3.4\ \text{mA h cm}^{-2}$ for 3.0, 3.2 and 3.5 V, respectively) were much lower than those of the liquid droplets. We propose that the different electrochemical performances of liquid and solid sulfur originate from differences in the kinetics of the liquid and solid states. Specifically, the liquid sulfur droplets do not hold on to a fixed position but rather readily move around on the MoS_2 flake. In addition, small sulfur droplets can merge into big ones and reduce the occupied area. Therefore, ‘fresh’ MoS_2 surfaces are continuously being exposed on which electrochemical reactions can continue to occur. As illustrated in Fig. 3c, after droplets 2 and 3 merge, new sites become available on which to generate new droplets. In contrast, the solid sulfur crystal is anchored to the MoS_2 surface with limited ability to diffuse or migrate. Exposed MoS_2 surfaces decrease over time and the area occupied by sulfur crystal is never re-exposed during charging. As illustrated in Fig. 3d, after the sulfur crystal covers the entire MoS_2 flake, the solid sulfur film blocks the electron transfer between polysulfide and MoS_2 due to the insulating nature of sulfur, which inhibits the electrochemical reaction.

As the applied voltage increased from 3.0 to 3.2 and then to 3.5 V, sulfur crystallized at 117, 79 and 32 s, respectively (corresponding to the turning points in the curves Fig. 3g). Faster sulfur crystallization

at higher voltages is consistent with our hypothesis that the electric field can induce heterogeneous nucleation and the crystallization of sulfur. In the meantime, we note that the areal capacities that we obtained for the liquid sulfur in this study are large. We suspect that some of the liquid sulfur droplets might be separated from the microelectrode due to the point contact of these droplets with the electrode as well as the dynamic generation of new droplets underneath. Additionally, we suspect that the metastable nature of liquid sulfur enables limited dissolution into the electrolyte, and as a result, strategies to host liquid sulfur droplets need to be developed for successful future electrode design. Liquid sulfur electrodes, however, hold great potential for flow battery systems³⁰ and fast-charging batteries.

Sulfur generation on other 2D materials

Finally, we examined other common 2D layered materials, including WS_2 , MoSe_2 , WSe_2 and graphite. We observed similar growth behaviour on these 2D transition-metal dichalcogenides and graphitic materials: solid sulfur crystal prefers to form on the edges of 2D flakes with large thickness, whereas liquid sulfur droplets generally grow on 2D flakes with small thickness (Fig. 4a–d and Supplementary Fig. 21). Analogous to monolayer MoS_2 , CVD-grown graphene only generates liquid droplets (Fig. 4e). Because the binding energy between S_8 and the edges is similar to that between S_8 and the basal plane of these 2D layered materials (Supplementary Table 1), we believe the electric field effect plays an important role, similarly to the case of MoS_2 . Raman spectroscopy confirmed the formation of sulfur on these materials (Fig. 4f). These observations,

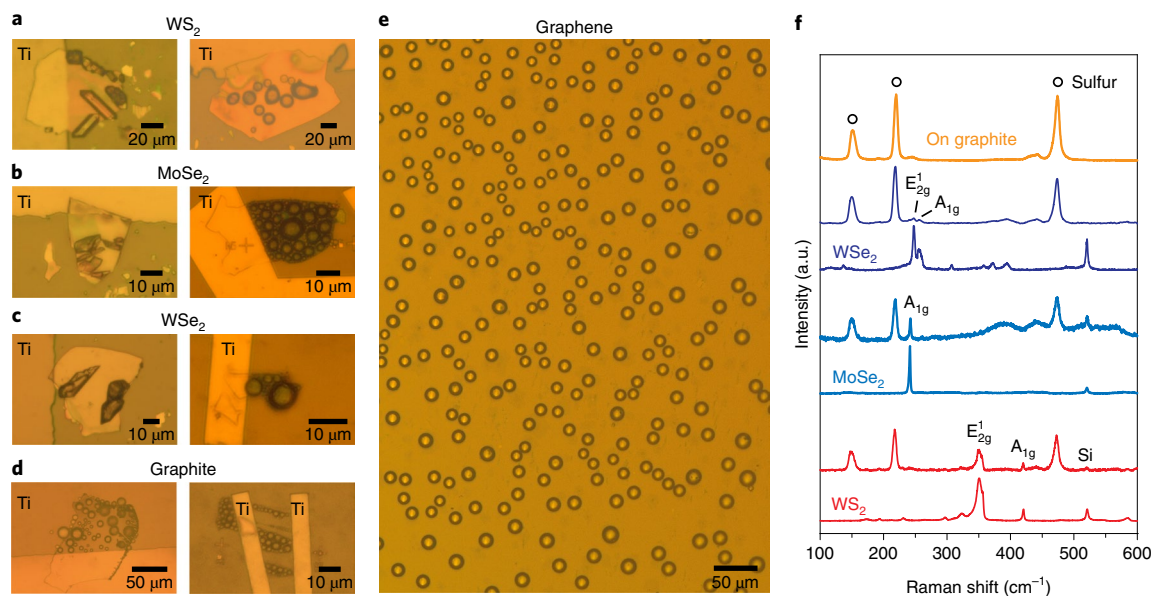


Fig. 4 | Sulfur generation on other 2D layered materials. **a–d**, Representative optical images of sulfur generation on 2D layered materials: WS₂ (**a**), MoSe₂ (**b**), WSe₂ (**c**) and graphite (**d**). Solid sulfur crystal grows from the edges of thick flakes and liquid sulfur droplets form on the basal plane of thin flakes. **e**, Liquid sulfur droplets generated on CVD-grown graphene. **f**, Raman spectra before (bottom) and after (top) sulfur generation on the 2D materials shown in **a–d**. From the bottom: red, WS₂; blue, MoSe₂; dark blue, WSe₂; orange, graphite after sulfur generation. Graphite itself does not show Raman features in the range 100–600 cm⁻¹.

together with those for MoS₂ (Fig. 1), show the universality of the sulfur growth phenomenon on 2D layered materials. Therefore, we believe that the results of this study demonstrate the application of 2D materials in Li–S batteries and will provide useful insights for the design of Li–S batteries.

Conclusions

We have reported here the first in situ study of the electrochemical generation of sulfur on 2D layered materials and have correlated the sulfur states with their electrochemical performances. Through in situ optical microscopy and Raman spectroscopy, we captured distinct sulfur growth behaviours on 2D materials, namely, liquid droplets grow on the basal plane of flakes and solid crystal grow from the edges of thick flakes. We have explained the different growth behaviours on the basis of binding energy, wetting ability, electric field distribution and critical nucleus size. Through simultaneous sulfur growth visualization and electrochemical measurements, we have successfully identified a correlation between sulfur state (liquid versus solid) and electrochemical performance. Liquid sulfur droplets can achieve much higher areal capacities than solid sulfur crystal over the same charge period. We hypothesize that liquid sulfur droplets enable faster kinetics due to their flowability and highly dynamic nature. In addition, the conversion between polysulfide and sulfur can change from a liquid/solid reaction to a liquid/liquid reaction, which holds promise for the design of flow-battery systems and fast-charging batteries. Finally, we have shown that the sulfur growth behaviour is relevant for a number of common 2D layered materials, thereby demonstrating the universality of the sulfur growth behaviour. These studies will shed light on electrode design for next-generation high-performance Li–S batteries.

Online content

Any methods, additional references, Nature Research reporting summaries, source data, extended data, supplementary information, acknowledgements, peer review information; details of author

contributions and competing interests; and statements of data and code availability are available at <https://doi.org/10.1038/s41565-019-0624-6>.

Received: 10 June 2019; Accepted: 12 December 2019;
Published online: 27 January 2020

References

- Bruce, P. G., Freunberger, S. A., Hardwick, L. J. & Tarascon, J.-M. Li–O₂ and Li–S batteries with high energy storage. *Nat. Mater.* **11**, 19–29 (2012).
- Seh, Z. W., Sun, Y., Zhang, Q. & Cui, Y. Designing high-energy lithium–sulfur batteries. *Chem. Soc. Rev.* **45**, 5605–5634 (2016).
- Zheng, G. et al. Amphiphilic surface modification of hollow carbon nanofibers for improved cycle life of lithium sulfur batteries. *Nano Lett.* **13**, 1265–1270 (2013).
- Yao, H. et al. Improving lithium–sulphur batteries through spatial control of sulphur species deposition on a hybrid electrode surface. *Nat. Commun.* **5**, 3943 (2014).
- Wang, H. et al. High electrochemical selectivity of edge versus terrace sites in two-dimensional layered MoS₂ materials. *Nano Lett.* **14**, 7138–7144 (2014).
- Liu, N. et al. Direct electrochemical generation of supercooled sulfur microdroplets well below their melting temperature. *Proc. Natl Acad. Sci. USA* **116**, 201817286–201817770 (2019).
- Nelson, J. et al. In operando X-ray diffraction and transmission X-ray microscopy of lithium sulfur batteries. *J. Am. Chem. Soc.* **134**, 6337–6343 (2012).
- Zhang, L., Sun, D., Feng, J., Cairns, E. J. & Guo, J. Revealing the electrochemical charging mechanism of nanosized Li₂S by in situ and operando X-ray absorption spectroscopy. *Nano Lett.* **17**, 5084–5091 (2017).
- Zhang, L. et al. The synergistic interaction between LiNO₃ and lithium polysulfides for suppressing shuttle effect of lithium-sulfur batteries. *Energy Storage Mater.* **11**, 24–29 (2018).
- Wu, Y. & Liu, N. Visualizing battery reactions and processes by using in situ and in operando microscopies. *Chem* **4**, 438–465 (2018).
- Stephenson, T., Li, Z., Olsen, B. & Mitlin, D. Lithium ion battery applications of molybdenum disulfide (MoS₂) nanocomposites. *Energy Environ. Sci.* **7**, 209–231 (2013).
- Ghazi, Z. A. et al. MoS₂/Celgard separator as efficient polysulfide barrier for long-life lithium–sulfur batteries. *Adv. Mater.* **29**, 1606817 (2017).

13. Lei, T. et al. Multi-functional layered WS₂ nanosheets for enhancing the performance of lithium–sulfur batteries. *Adv. Energy Mater.* **7**, 1601843 (2017).
14. Seh, Z. W. et al. Two-dimensional layered transition metal disulphides for effective encapsulation of high-capacity lithium sulphide cathodes. *Nat. Commun.* **5**, 5017 (2014).
15. Babu, G., Masurkar, N., Salem, Al. H. & Arava, L. M. R. Transition metal dichalcogenide atomic layers for lithium polysulfides electrocatalysis. *J. Am. Chem. Soc.* **139**, 171–178 (2016).
16. Zhang, Q. et al. Understanding the anchoring effect of two-dimensional layered materials for lithium–sulfur batteries. *Nano Lett.* **15**, 3780–3786 (2015).
17. Wang, H. et al. Graphene-wrapped sulfur particles as a rechargeable lithium–sulfur battery cathode material with high capacity and cycling stability. *Nano Lett.* **11**, 2644–2647 (2011).
18. Ji, L. et al. Graphene oxide as a sulfur immobilizer in high performance lithium/sulfur cells. *J. Am. Chem. Soc.* **133**, 18522–18525 (2011).
19. Chen, H. et al. High-quality graphene microflower design for high-performance Li–S and Al-ion batteries. *Adv. Energy Mater.* **7**, 1700051 (2017).
20. Su, D., Cortie, M. & Wang, G. Fabrication of N-doped graphene–carbon nanotube hybrids from Prussian blue for lithium–sulfur batteries. *Adv. Energy Mater.* **7**, 1602014 (2017).
21. Choi, S. et al. WO₃ nanolayer coated 3D-graphene/sulfur composites for high performance lithium/sulfur batteries. *J. Mater. Chem. A* **7**, 4596–4603 (2019).
22. Sun, J. et al. Entrapment of polysulfides by a black-phosphorus-modified separator for lithium-sulfur batteries. *Adv. Mater.* **28**, 9797–9803 (2016).
23. Nims, C., Cron, B., Wetherington, M., Macalady, J. & Cosmidis, J. Low frequency Raman spectroscopy for micron-scale and in vivo characterization of elemental sulfur in microbial samples. *Sci. Rep.* **9**, 1–12 (2019).
24. Pascal, T. A. et al. X-ray absorption spectra of dissolved polysulfides in lithium–sulfur batteries from first-principles. *J. Phys. Chem. Lett.* **5**, 1547–1551 (2014).
25. Levin, B. D. A. et al. Characterization of sulfur and nanostructured sulfur battery cathodes in electron microscopy without sublimation artifacts. *Microsc. Microanal.* **23**, 155–162 (2017).
26. Kim, H. et al. In situ TEM observation of electrochemical lithiation of sulfur confined within inner cylindrical pores of carbon nanotubes. *Adv. Energy Mater.* **5**, 1501306 (2015).
27. Hamada, S., Nakazawa, Y. & Shirai, T. Nucleation in liquid sulfur droplets. *Bull. Chem. Soc. Jpn.* **43**, 3096–3101 (2006).
28. Mugele, F. & Baret, J.-C. Electrowetting: from basics to applications. *J. Phys.: Condens. Matter* **17**, R705–R774 (2005).
29. Pollack, M. G., Fair, R. B. & Shenderov, A. D. Electrowetting-based actuation of liquid droplets for microfluidic applications. *Appl. Phys. Lett.* **77**, 1725–1726 (2000).
30. Yang, Y., Zheng, G. & Cui, Y. A membrane-free lithium/polysulfide semi-liquid battery for large-scale energy storage. *Energy Environ. Sci.* **6**, 1552–1558 (2013).

Publisher's note Springer Nature remains neutral with regard to jurisdictional claims in published maps and institutional affiliations.

© The Author(s), under exclusive licence to Springer Nature Limited 2020

Methods

Device fabrication. MoS₂ flakes were deposited on 300-nm-thick SiO₂/Si substrates by either directly exfoliating MoS₂ crystals using the Scotch tape method or transferring CVD-grown monolayer MoS₂ using poly(methyl methacrylate). WS₂, MoSe₂, WSe₂, and graphite were exfoliated from the corresponding crystals. Graphene was CVD-grown on copper and then transferred onto SiO₂/Si substrates. The electrodes were defined on flakes by electron beam lithography (JEOL JBX-6300FS) followed by titanium deposition (80–100 nm). For the devices in Fig. 3, an additional 120-nm layer of SiO₂ was deposited by high-density plasma-enhanced CVD (Plasma-Therm VERSALINE) to cover the titanium electrodes. The device was then transferred to an argon-filled glovebox for cell assembly. The 2D flakes were used as the working electrode and lithium metal cold-pressed on a copper foil was used as the counter electrode. A cover glass slide was placed on top of the electrodes and the cell was then sealed with a thermoplastic film (Meltonix 1170-60, Solaronix) leaving two small openings for filling with the liquid electrolyte. Here, Li₂S₈ dissolved in 1,3-dioxolane/1,2-dimethoxyethane (1:1, v/v) with 1 M lithium bis(trifluoromethanesulfonyl)imide and 1 wt% LiNO₃ additive was used as the catholyte (0.5 or 5 M). After filling with the electrolyte, the two openings were sealed by epoxy.

In situ observation of sulfur generation on 2D materials. The in situ electrochemical reaction was performed with an MTI eight-channel battery tester or a Bio-Logic potentiostat and was imaged simultaneously using a light microscope equipped with an air-immersion objective (LMPLFLN-BD, Olympus), broadband xenon lamp and complementary metal oxide semiconductor detector. The images were taken at a frame rate of 1 frame s⁻¹ and the spatial resolution of the microscope was ~500 nm. Constant voltage charging was used to generate sulfur, with galvanostatic discharging to dissolve sulfur.

Device characterizations. *Raman spectroscopy.* A HORIBA Scientific LabRAM HR Evolution spectrometer was used for Raman spectroscopy with 532 or 633 nm excitation and a 1,800 grooves mm⁻¹ grating. A half waveplate optimized at 633 nm was inserted before the objective to rotate the laser polarization and perform polarized Raman spectroscopy.

Atomic force microscopy. A Park XE-70 microscope in non-contact mode was used for AFM.

Transmission electron microscopy. An FEI Tecnai microscopy with an operating voltage of 200 kV was used for TEM.

Cryo-electron microscopy. Sulfur grown on a nickel TEM grid was plunge-frozen in liquid nitrogen and mounted onto a cryogenic TEM holder (Gatan) cooled to liquid nitrogen temperatures. The TEM holder was then transferred into the column of the TEM (FEI Titan, 300 kV) at which point the temperature of the TEM grid was stabilized at -175 °C. To prevent damage to the crystal structure, all images and diffraction patterns were collected using a low dose rate of 0.05 e⁻ Å⁻² s⁻¹.

X-ray absorption near-edge structure spectroscopy. Sulfur K-edge XANES spectroscopy measurements were carried out at the XFM beamline 10.3.2 of the Advanced Light Source, Lawrence Berkeley National Laboratory. All data were collected in fluorescence mode using an Amptek C2 detector. An air-exclusion chamber purged with helium gas was placed in the path between the sample and the detector. Data were collected in QXAS mode, with the monochromator scanned on the fly from 2,440 to 2,540 eV in steps of 0.2 eV around the sulfur K-edge. The QXAS mode allowed us to monitor any potential beam damage. Spectra were recorded using a beam spot size of 6 μm × 2.5 μm. XANES spectra were calibrated using the main peak of gypsum (CaSO₄) at 2,482.75 eV. The spectra were deadtime-corrected, deglitched, calibrated and background-subtracted using a spectrum recorded in the absence of a sample. Data were processed using a suite of custom LabVIEW software available at the beamline and then pre-edge background-subtracted and post-edge normalized using Demeter Athena software³¹.

DFT calculations. Calculations from first principles were performed using DFT within the general gradient approximation (GGA) in the form of the Perdew–Burke–Ernzerhof's exchange–correlation functional. The D2 method of Grimme was added as a correction term to take into consideration van der Waals interactions. All calculations were performed using the Vienna Ab initio Simulation Package (VASP).

Molecular dynamics simulations. MD simulations were conducted using the Large-scale Atomic/Molecular Massively Parallel Simulator (LAMMPS)³². We used a transferable atomistic force field to describe MoS₂ (ref. 33) and a newly developed and well-benchmarked force field to describe the polysulfide³⁴. The composition of the electrolyte was set based on the experimental setting. (1) The constant potential simulation method³⁵ was used to study the atomic charges on the MoS₂ electrode. In this method, the atomic charges on the electrodes were allowed to fluctuate to give the desired constant potential on the electrodes³⁶. To guarantee the stability of the algorithm and the calculation efficiency, two identical MoS₂ structures were

placed in the simulation box at a distance of 6 nm in mirror symmetry with respect to their centre plane. The two MoS₂ electrodes bear a potential of -1.5 and 1.5 V, respectively, giving a voltage drop of 3.0 V, matching that of the experimental setting. In our analysis, we only focused on the positive MoS₂ electrode. Periodic boundary conditions were used in parallel directions and wall boundaries were used for the top and bottom of the box. The slab particle mesh Ewald (PME) method was used to compute electrostatic interactions. During the simulation, the electrode atoms and box dimensions were fixed. (2) For the wetting ability simulations, MoS₂ slabs with different surfaces were cut from crystals along different directions to reflect the basal plane and the edges. An assembly of 290 cyclic S₈ molecules was placed 0.5 nm above the two different MoS₂ substrates. The MoS₂ slabs and sulfur droplets were then immersed in electrolyte. We first conducted a 200-ps simulation with both MoS₂ substrate and S₈ aggregates fixed to relax the electrolyte. Periodic boundary conditions were applied along all three directions. During the simulation, the box was allowed to change in the z direction to give the desired pressure of 1 bar. To characterize the wetting property of sulfur droplets on different surfaces, we took a snapshot at 2 ns for comparison.

Electric field simulations. A 3D model was built using the AC/DC physics module in COMSOL Multiphysics. A flake of MoS₂ with dimensions 20 μm × 5 μm × 100 nm (length × width × height) was placed between two electrodes spaced 30 μm apart. Voltages of 3.0, 3.2 and 3.5 V were applied to the MoS₂ side and the other side was grounded. The surrounding media was set as ether-based lithium ion battery electrolyte, with a relative permittivity of 7, and MoS₂ had a relative permittivity of 16 (ref. 37). The steady-state potential distribution was calculated and the electric fields were plotted as shown.

Data availability

The data that support the plots within this paper and other findings of this study are available from the corresponding author upon reasonable request.

References

- Ravel, B. & Newville, M. ATHENA, ARTEMIS, HEPHAESTUS: Data Analysis for X-Ray Absorption Spectroscopy Using IFEFFIT. *J. Synchrotron Radiat.* **12**, 537–541 (2005).
- Plimpton, S. Fast parallel algorithms for short-range molecular dynamics. *J. Comput. Phys.* **117**, 1–19 (1995).
- Sresht, V. et al. Quantitative modeling of MoS₂-solvent interfaces: predicting contact angles and exfoliation performance using molecular dynamics. *J. Phys. Chem. C* **121**, 9022–9031 (2017).
- Rajput, N. N. et al. Elucidating the solvation structure and dynamics of lithium polysulfides resulting from competitive salt and solvent interactions. *Chem. Mater.* **29**, 3375–3379 (2017).
- Merlet, C. et al. On the molecular origin of supercapacitance in nanoporous carbon electrodes. *Nat. Mater.* **11**, 306–310 (2012).
- Wang, Z., Yang, Y., Olmsted, D. L., Asta, M. & Laird, B. B. Evaluation of the constant potential method in simulating electric double-layer capacitors. *J. Chem. Phys.* **141**, 184102 (2014).
- Laturia, A., Van de Put, M. L. & Vandenberghe, W. G. Dielectric properties of hexagonal boron nitride and transition metal dichalcogenides: from monolayer to bulk. *npj 2D Mater. Appl.* **2**, 4106 (2018).

Acknowledgements

We acknowledge support from the Department of Energy, Office of Basic Energy Sciences, Division of Materials Science and Engineering under contract DE-AC02-76SF00515. Part of this work was performed at the Stanford Nano Shared Facilities (SNSF) and Stanford Nanofabrication Facilities (SNF), supported by the National Science Foundation under award ECCS-1542152. R.A.V. acknowledges support from the National Academy of Sciences Ford Foundation Fellowship and the National Science Foundation Graduate Research Fellowship Program (NSF GRFP, grant number: DGE-1656518). We acknowledge C. Su and J. Li from MIT for performing the DFT calculations. A.Y. acknowledges D. Zakhidov for his assistance with polarized Raman measurements and Y. Ye, Z. Wang and R. Xu for helpful discussions.

Author contributions

A.Y. and Y.C. conceived and designed the experiments. A.Y. and G.Z. carried out device fabrication, imaging and electrochemical measurements. X.K. and J.Q. performed MD simulations. R.A.V. performed TEM characterizations. A.P. performed COMSOL simulations. X.Z. and S.F. performed in situ XAS measurements. Y.W., C.-L.W. and B.L. assisted in material preparation. X.Y., H.C., Y.X., D.C. and Y.L. assisted in electrochemical measurements. H.Y.H., S.C. and Y.C. supervised the project and all authors contributed to data discussions. A.Y. and Y.C. analysed the data and wrote the paper with input from all authors.

Competing interests

The authors declare no competing interests.

Additional information

Supplementary information is available for this paper at <https://doi.org/10.1038/s41565-019-0624-6>.

Correspondence and requests for materials should be addressed to Y.C.

Peer review information Nature Nanotechnology thanks Yuyan Shao, Guoxiu Wang and Reza Shahbazian-Yassar for their contribution to the peer review of this work.

Reprints and permissions information is available at www.nature.com/reprints.